Ultramicroscopy 239 (2022) 113561

Contents lists available at ScienceDirect

Ultramicroscopy

journal homepage: www.elsevier.com/locate/ultramic

High-precision atomic-scale strain mapping of nanoparticles from STEM images

Xiaonan Luo [a], Aakash Varambhia [b], Weixin Song [a], Dogan Ozkaya [b], Sergio Lozano-Perez [a], Peter D. Nellist [a,*]

[a] Department of Materials, University of Oxford, Parks Road, OX1 3PH, Oxford, United Kingdom
[b] Johnson Matthey Technology Centre, Sonning Common, RG4 9NH, Reading, United Kingdom

ARTICLE INFO

Keywords:
Strain
Nanoparticle
Differential displacement
Pt-Co catalyst
Lattice parameter
Scanning transmission electron microscopy

ABSTRACT

Strain is a crucial factor that influences the physicochemical properties of nanoparticles. Being able to precisely measure strain is important in understanding the intrinsic mechanism of the enhanced performance of nanoparticles. Techniques that have been developed for strain analysis using scanning transmission electron microscopy (STEM) images can be categorized into diffraction-based method and imaging-based method. Here, using image simulation techniques, it is found that the measured two-dimensional (2D) displacements from annular dark field (ADF) STEM images of a nanoparticle are a good approximation to a projection of the actual three-dimensional (3D) displacements. A methodology for deformation analysis is presented which is based on the detection of atomic columns from atomic-resolution STEM images in real space. Elastic deformation parameters such as strain are usually defined on the basis of a continuum of deformation. The appropriateness of various deformation parameters for atomic-scale investigation on STEM images is explored and a method for determining these is presented. We found that the local lattice parameter and principal strain components are the most physically meaningful parameters to express the materials distortion behaviour. Apart from the local lattice parameter, the other deformation parameters such as normal strains, shear strains and displacements, heavily rely on the choice of reference lattice. It is also found that different reference grids add a series of uniform offsets to these strain variations. Finally, this approach is applied to a $PtCo_3$ bimetallic nanoparticle to quantify its deformation behaviour.

1. Introduction

Nanoparticles have been widely used as catalysts in applications including clean energy systems and gaseous pollutant purification due to excellent physicochemical properties compared to their bulk counterparts [1-3]. Previous work has shown that the enhanced performance of nanoparticles is dependant on structure, morphology, composition, and size [4-6]. The finite size, morphology, and lattice mismatch between different elements can induce strain that results in modification of the electronic structure [7-14]. The strain has also been shown to be related to the catalytic activity of nanoparticles through density functional theory (DFT) calculations [15]. As strain is believed to play a significant role in understanding the intrinsic mechanism behind the improved catalytic activity, it needs to be measured precisely [16].

A number of methods have been developed for deformation mapping with a transmission electron microscope. The methodologies can be classified into two categories: diffraction-based and imaging-based methods. The former method is based on measuring displacements from diffraction patterns in reciprocal space, including convergent-beam electron diffraction (CBED) and nano-beam electron diffraction (NBED). The imaging-based methods quantify the displacement of atomic columns or lattice fringes from high-resolution images in real space. Imaging-based techniques can further be categorized into four different approaches, Geometric Phase Analysis (GPA), Dark Field Electron Holography (DFEH), Peak Pair (PP), and Peak Finding (PF).

Diffraction-based techniques are presently of widespread use in the semiconductor industry [17]. The CBED approach provides strain profiles by measuring the position shifts of the dark High Order Laue Zone (HOLZ) lines [18,19]. Although it can achieve good spatial resolution ($0.5 - 2\ nm$) and high sensitivity to strain, HOLZ lines are not detectable in the diffraction patterns on thin samples such as nanoparticles [20]. The NBED approach uses a near-parallel nanometre-sized

* Corresponding author.
E-mail address: peter.nellist@materials.ox.ac.uk (P.D. Nellist).

https://doi.org/10.1016/j.ultramic.2022.113561
Received 20 December 2021; Received in revised form 2 May 2022; Accepted 21 May 2022
Available online 22 May 2022

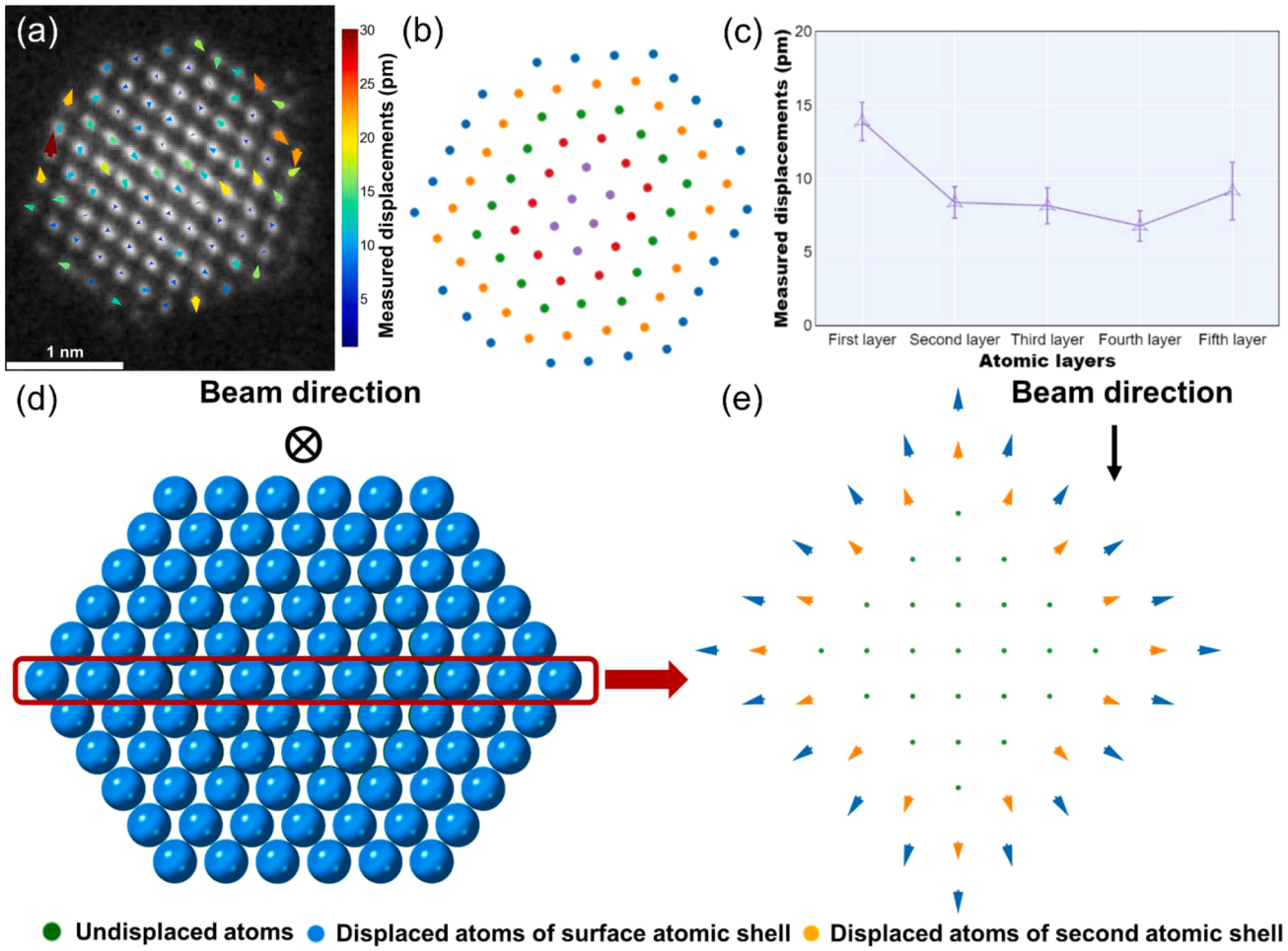

Fig. 1. (a) The displacement map from an experimental Pt nanoparticle. (b) Atomic columns colour coded with each 2D projected atomic layer. The outermost layer (blue) is the first atomic layer and the core (purple) is the fifth atomic layer. (c) Plot of the average magnitude of the measured displacements as a function of each atomic layer from the experimental image. (d) The perfect cuboctahedra Pt 3D model with the outermost atomic shell coloured blue. This nanoparticle model is aligned along the [110] direction (beam direction). (e) The middle atom plane from the nanoparticle model in (d), where atoms in two outer atomic shells are displaced (shown as arrows).

beam to form diffraction patterns [21,22]. The deformation field is determined by comparing the diffraction pattern of each probe position with a reference pattern [17]. However, this approach cannot provide site-specific atomic-resolution strain measurements. Additionally, both CBED and NBED techniques broaden the diffraction spots into discs. Each diffraction disc results from a combination of both single scattering electrons and multiple scattering electrons. Dynamical electron scattering can change the intensity distribution within the diffraction discs [23], The resultant non-uniform intensity in the discs affects the determination of scattering angles. In other words, the scattering angles measured from the diffraction discs do not always correspond to the atom planes that we want to measure [20].

The DFEH approach tries to overcome the precision limitation by using an electron biprism to interfere the diffracted beams from the region of interest and a reference area [24]. The phase difference in the interference pattern is used to calculate the strain tensor. Although its spatial resolution can reach 1 nm in principle [25], a specimen with both a non-strained and a strained area is required, which is impossible for nanoparticles. The GPA methodology works by demodulating the lattice fringes associated with a selected Bragg spot giving a phase map that describes the deformation. The strain tensor is obtained from the displacements determined from two non-collinear Bragg spots [26]. This approach is extensively used in strain measurements of materials that contain defects [27], however it is not possible to obtain atomic site-specific strain maps due to a spatial resolution of ~1 nm.

To measure strain at atomic resolution the most promising approaches are PF and PP. Both the PF and PP approaches are based on the real-space position detection of atomic columns directly from the experimental images [28-31]. In the PF methodology, a reference grid is extrapolated from what is assumed to be a non-strained area of the sample and cast over the deformed region. The discrete displacement field at each atomic column is calculated to obtain the strain field. For the PP approach, two non-collinear basis vectors are defined using a reference lattice. A pair of peaks at each atomic column are located along the two basis vector directions. The local strain field is determined by comparing pairs of peaks with reference atom-to-atom bond lengths. Regardless of the differences between the PF and PP methods, both techniques require a non-strained reference area in the field of view, which may not be a good assumption for small nanoparticles. Unlike bulk materials, the deformation can be distributed throughout the whole nanoparticle due to the finite size and domain structure. These two methods are sensitive to errors in the formation of a reference lattice.

Apart from the intrinsic limitations of all the imaging-based methods discussed here, the projection approximation also need to be carefully considered. Strain mapping on the STEM images is 2D, but the actual strain distribution within the specimen is 3D and not always uniform along the viewing direction. Because of this limitation any local strain measured via imaging techniques cannot always fully express the real

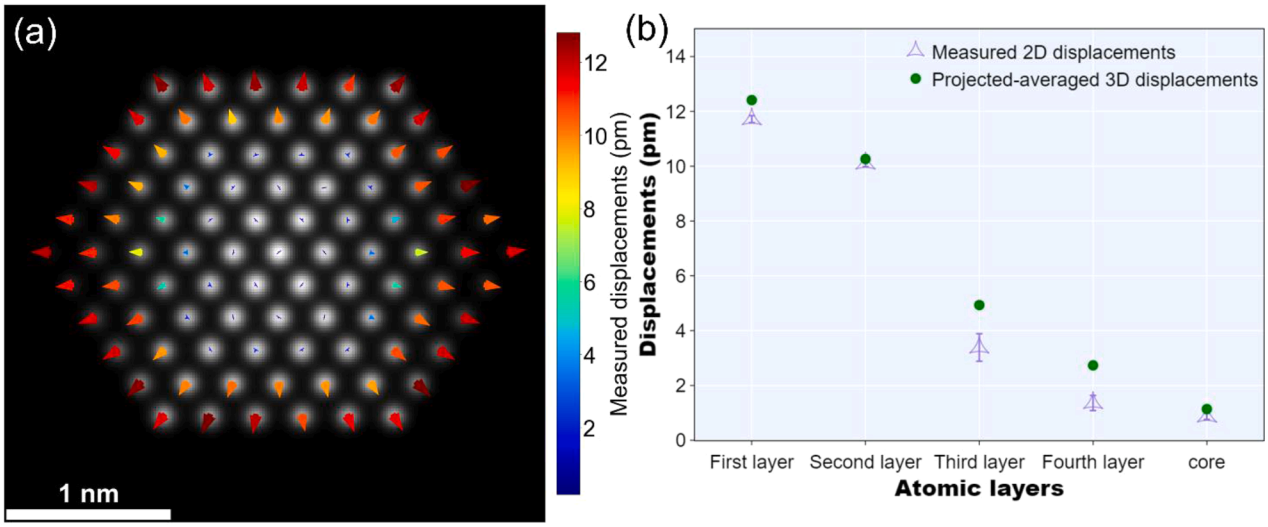

Fig. 2. (a) The displacement map of the strained Pt model. (b) The average magnitude of the measured displacements as a function of the atomic layer, the error bar is displayed as the standard error of each atomic layer.

3D distortion behaviour of the sample [20]. Here, we investigate, to what extent the measured displacements from the ADF STEM images match the in-plane components of the displacement averaged through the thickness.

While characterising the distortion behaviour of materials is of great importance, the deformation parameters quantified within the literature are inconsistent. Material deformation parameters such as strain have usually been defined on a continuum basis [17-22,24-26,28,32-35]. However, for atomic-resolution images of nanoparticles, material deformation should be defined on the discrete atomic columns. Material distortions have been described using the following deformation parameters: the displacement vector [7,29], the local lattice parameter [16,36], some or all of the strain components [28,32] and occasionally also including the lattice rotation [26]. The two dimensional strain tensor consists of two normal strain components and one shear strain component. Rotation of the coordinate axes on which these are defined, for example by applying the Mohr's circle construction, can change the strain components with normal strains converting into shear strains and vice-versa. Rarely in previous work has the full strain tensor been presented. Here, the relevance and usefulness of various elastic displacement parameters are considered in the context of atomic resolution with the aim of identifying a physically meaningful parameter that can be related to other measurements and modelling.

In this work, the validity of the projection approximation is first studied using STEM imaging simulation. To precisely measure the strain field, an algorithm based on locating atomic columns in real space is presented. Our methodology is robust enough to be applied to strain mapping on both nanoparticles and bulk materials with defects, dislocations and interfaces. Next, the materials deformation parameters defined on a 2D primitive cell are compared and the relationship between them is investigated. Differences of strain mapping using different reference lattices are then discussed. In addition, the influence from Poisson noise on strain measurements is studied. Finally, the application of this methodology in the experimental nanoparticles is demonstrated by quantifying the displacement fields, the local lattice parameters, and the strain fields on a $PtCo_3$ bimetallic nanoparticle.

2. Validity of projection approximation for displacements

For atomic-resolution imaging, nanoparticles are viewed along a low-order zone axis in the microscope. The obtained STEM image is generally interpreted as the 2D projection of the 3D sample. The distortion distribution of the nanoparticle is always 3D and is never uniform along the viewing direction. The question then arises of whether the displacements of atomic columns measured in a 2D image can be interpreted as the components (perpendicular to the beam) of the 3D atomic displacements averaged along the column. The effects of dynamical electron scattering and the resultant channelling of the beam may preclude such a simple interpretation. Here, the influence from the 2D projection approximation on the displacement measurements from the ADF STEM images is investigated.

To create a nanoparticle model containing strain, we used a perfect zero-strain cuboctahedra Pt 3D model with a diameter of 2.5 nm and bulk lattice parameter of 0.39231 nm at 280 K [37], as shown in Fig. 1d, and displacements with similar magnitudes to those measured experimentally were artificially added to the perfect 3D model. The experimental displacements were measured from an ADF image of an experimental Pt nanoparticle with a diameter of ~2.5 nm, which is similar to the model, using our proposed methodology described in Section 3, as shown in Fig. 1a. The experimental ADF image comes from the previously published work by Aarons, et al. [14]. For the 3D nanoparticle model, the atomic shells are defined as a series of one-atom-thick 3D hollow shells, moving from the nanoparticle surface to its centre. The outermost atomic shell is composed of all surface atoms in the 3D nanoparticle model. Each atomic column in Fig. 1d, which is a projection, could have atoms from different atomic shells of the model. We use the term "atomic layers" as rings of atomic columns in the 2D image of the nanoparticle model projected along the beam direction in Fig. 1d, starting from the surface and moving in towards the centre. Thus, there are six atomic layers in Fig. 1d, where the sixth atomic layer only has a centre atomic column. Fig. 1c displays the measured displacement as a function of the atomic layer of the experimental nanoparticle defined in Fig. 1b, where the average displacement of atomic columns in the surface layer is measured to be ~13 pm. To create the strained Pt 3D model, the atoms in the outermost atomic shell of the perfect Pt 3D model are radially displaced relative to their original positions by the same amount (13 pm), while the second outer atomic shell displacement is calculated by scaling the added surface displacement with respect to the shell radius to give a displacement of 10.5 pm. The rest of atoms in this nanoparticle model remain undisplaced to provide a relatively simple model which captures our general observations that most strain is observed in the outer layers. Fig. 1e shows the middle atom plane of the Pt nanoparticle model along the beam direction. In the selected atom plane, the atoms in the two outer atomic shells have been displaced (shown as arrows). As the result, atomic columns along the beam direction have a curved shape.

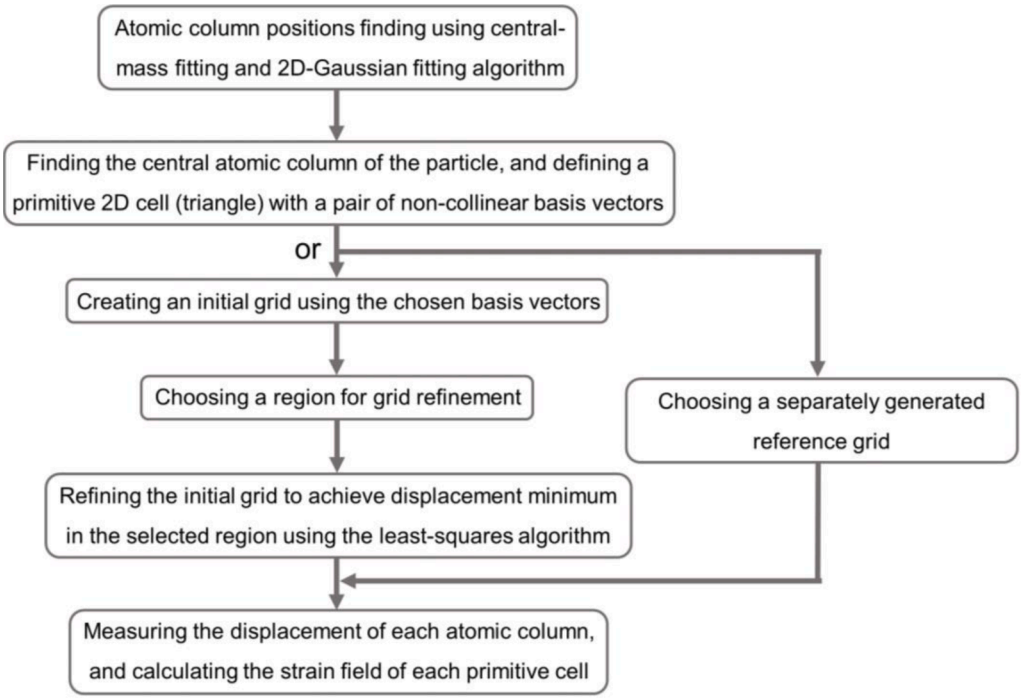

Fig. 3. Flow diagram of the deformation analysis algorithm.

The high-resolution ADF STEM images of both the perfect and strained Pt 3D models along [110] direction were simulated using the MULTEM software [38]. The simulation voltage was set to 200 kV with a source size broadening value of 0.8Å. The probe convergence angle was set as 22.48 mrad whereas the ADF detector collection angles spanned from 72.8 to 271 mrad. The multislice frozen phonon calculation was performed using the Einstein model with 50 phonon configurations and a root mean square (RMS) displacement of 0.06917 Å derived from the Debye-Waller factor of the Pt bulk materials [39].

A 2D Gaussian function was then fitted to each atomic column in the simulated image of the strained Pt model using the ATOMAP software [40], yielding the 2D coordinates. The 3D coordinates of the perfect model without strain are projected along the [110] direction, yielding a 2D reference grid. The displacement map extracted from the strained model was calculated by measuring the distances between the observed positions of atomic columns and the corresponding reference point positions, as shown in Fig. 2a. It is clear that the measured displacements are symmetrically distributed and the atoms of the outer two atomic layers are displaced outward from the nanoparticle. The measured 2D displacements from the simulated image were then compared with the averaged-projected real 3D displacements calculated using the coordinates of the 3D strained model, as shown in Fig. 2b. Here, the atomic core is defined as all the atomic columns in the fifth and sixth atomic layers. Overall, the measured 2D displacements follow the projected-averaged 3D displacements well. For the outer two atomic layers, there is minimal difference between the measured and real 2D displacements. However, for the inner atomic layers, some discrepancies are detected. The maximum difference between the measured and real 2D displacement is within 1.5 pm. This inconsistency comes from the so-called 'channelling effect' [41] where the atoms that are close to being aligned have a disproportionately stronger scattering effect. The well-aligned middle undisplaced atoms (green atoms in Fig. 1e) have more influence on the atomic column position detection compared to the mis-aligned displaced atoms in the two outer atomic shells. The influence from the 'channelling effect' are reduced as the atomic column gets thicker because the averaged-projected displacement vectors will be smaller as the undisplaced core atoms dominate. We can therefore expect the smaller nanoparticle to have more columns in an image that suffer from the 'channelling effect' than the larger one in terms of the discrepancy between the measured 2D and projected actual 3D displacements, hence the use in the simulation is the nanoparticle with a diameter of 2.5 nm.

In general, the projection approximation for displacement measurements on the ADF STEM image is found to be reasonable for nanoparticles. For the nanoparticle simulated here, the maximum error in displacement measurements is found to be 1.5 pm. This is sufficiently small to allow the application of this approach to understand the 2D projection of the actual 3D distortion behaviour of the nanoparticle.

3. Defining and measuring strain at the atomic scale

The overall proposed methodology for nanoparticle strain analysis is based on the detection of atomic columns in the atomic-resolution images, similar to the PF and PP approaches. Fig. 3 shows an outline of the methodology used in this work. For STEM image acquisitions, the multi-frame imaging technique is used to reduce the influence of scan instabilities and drift [42]. The acquired experimental atomic-resolution ADF image frames of an on-axis nanoparticle are aligned using non-rigid registration method and averaged to obtain a zero-drift ADF image [43]. The following step is to locate the positions of all the atomic columns that are of interest in the aligned ADF image. The initial positions are detected using the peak finding algorithm implemented in the ATOMAP Python library, where the relative intensity threshold and the smallest peak separation are taken as inputs. The initial positions are further refined first by finding the centre of mass and then by fitting of 2D Gaussian peak to each atomic column. This allows us to precisely determine the 2D coordinates of the atomic column positions.

Next, the centre atomic column and its nearest neighbouring columns are found to determine a primitive 2D cell (a parallelogram) defined by two non-collinear basis vectors (**a** and **b**). Let us consider FCC crystal structure down a [110] projection, as shown in Fig. 4b. The centre atomic column and its six neighbouring columns form six triangles, and each of them can be used to define the two basis vectors.

The following step is the selection of a reference grid. The reference grid can be a separately generated either from a bulk material with known lattice constants, or from a region of the nanoparticle. The

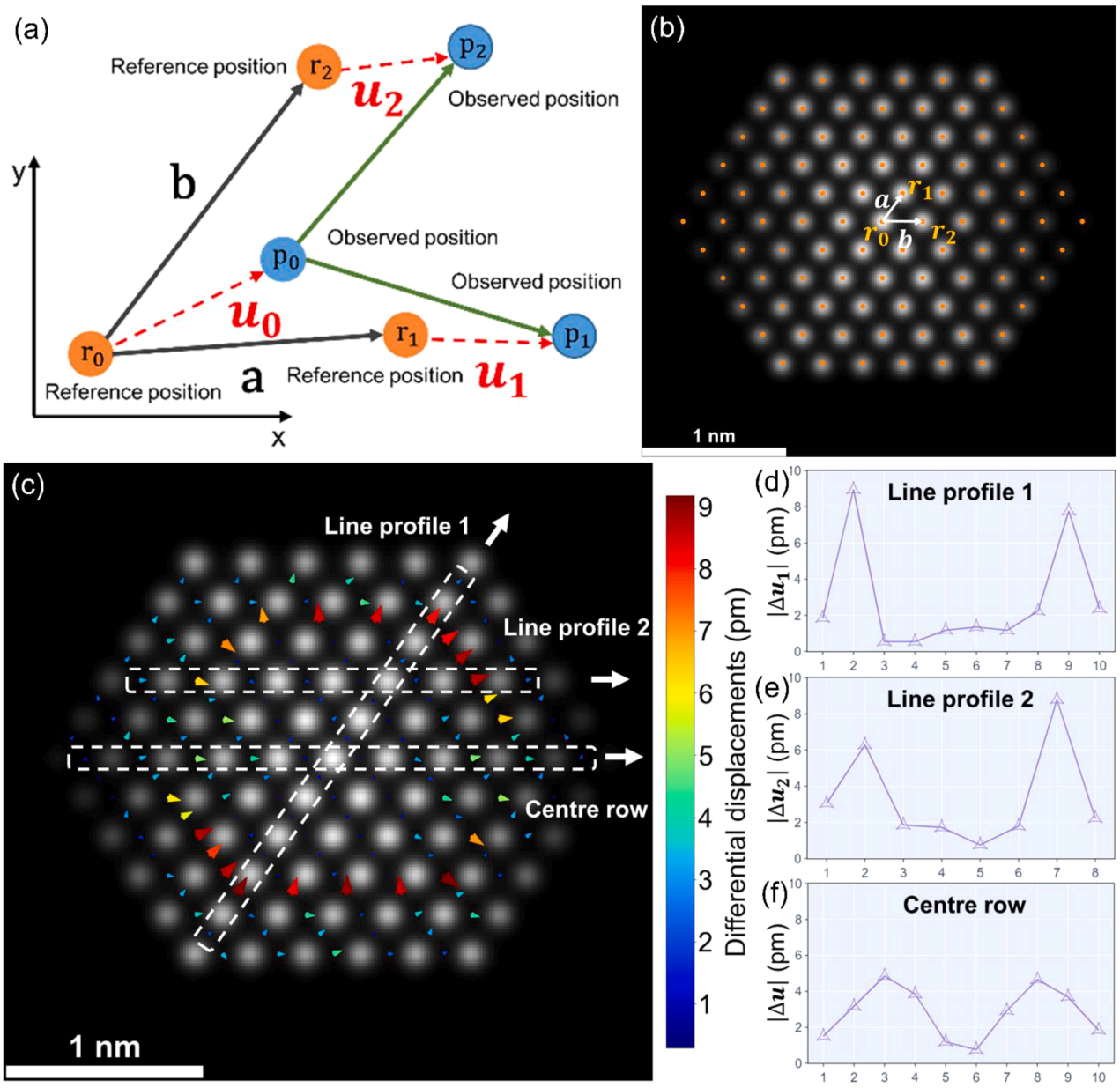

Fig. 4. (a) Diagram of the definition of the local displacement vectors. (b) The reference primitive unit of the strained Pt model. (c) The differential displacement map of the strained Pt model. (d-f) The selected line profiles in (c) of the differential displacements $|\Delta \boldsymbol{u}_1|$, $|\Delta \boldsymbol{u}_2|$ and $|\Delta \boldsymbol{u}|$ (pm).

differences of using the different reference grids for strain mapping will be compared and discussed in the following section. To create a reference grid from the nanoparticle, an initial reference grid is first generated using the initial basis vectors. The next step is to choose a region to refine the initial reference grid. The selected region can be either the whole particle or a part of the particle. Then, the initial grid is contracted, expanded, rotated, and offset to achieve the displacement minimum in the selected region using a least-squares fitting algorithm. The reference basis vectors and the reference triangles are extracted from the refined reference grid.

On the basis of having the atomic column positions and the reference grid, all the observed triangles and the reference triangles in the region of interest are searched. Subsequently, the displacement vector of each atomic column is measured. The local differential displacement and the strain tensor of each triangle unit are extracted from the displacement field. This step is the most novel part of this methodology, and will be discussed in detail.

Materials deformation parameters such as elastic strain are often associated with continuum elasticity. When dealing with nanoparticles where the discrete atomic nature becomes important, it is important to consider which deformation parameters are appropriate. In order to investigate this, the following deformation descriptors were calculated on the simulated image of the strained Pt model. The reference grid is still the projection along the [110] direction of the perfect Pt model without strain. We start with the local displacement vector $\boldsymbol{u}_i$ that is associated with each atomic column in the image. The displacement vector is defined by the position offset of each observed atomic column with respect to the closest reference point, as shown in Fig. 4a. If we consider a triangle formed from the primitive basis vectors in the projected 2D lattice, we can define the differential displacement field, the strain field, the fractional area expansion and the local lattice parameter. The non-collinear basis vectors ($\boldsymbol{a} = (a_x, a_y)$ and $\boldsymbol{b} = (b_x, b_y)$) and the 2D primitive triangle ($r_0 r_1 r_2$) of the reference grid are defined in Fig. 4b.

The differential displacement field Δu is first introduced by the following equations:

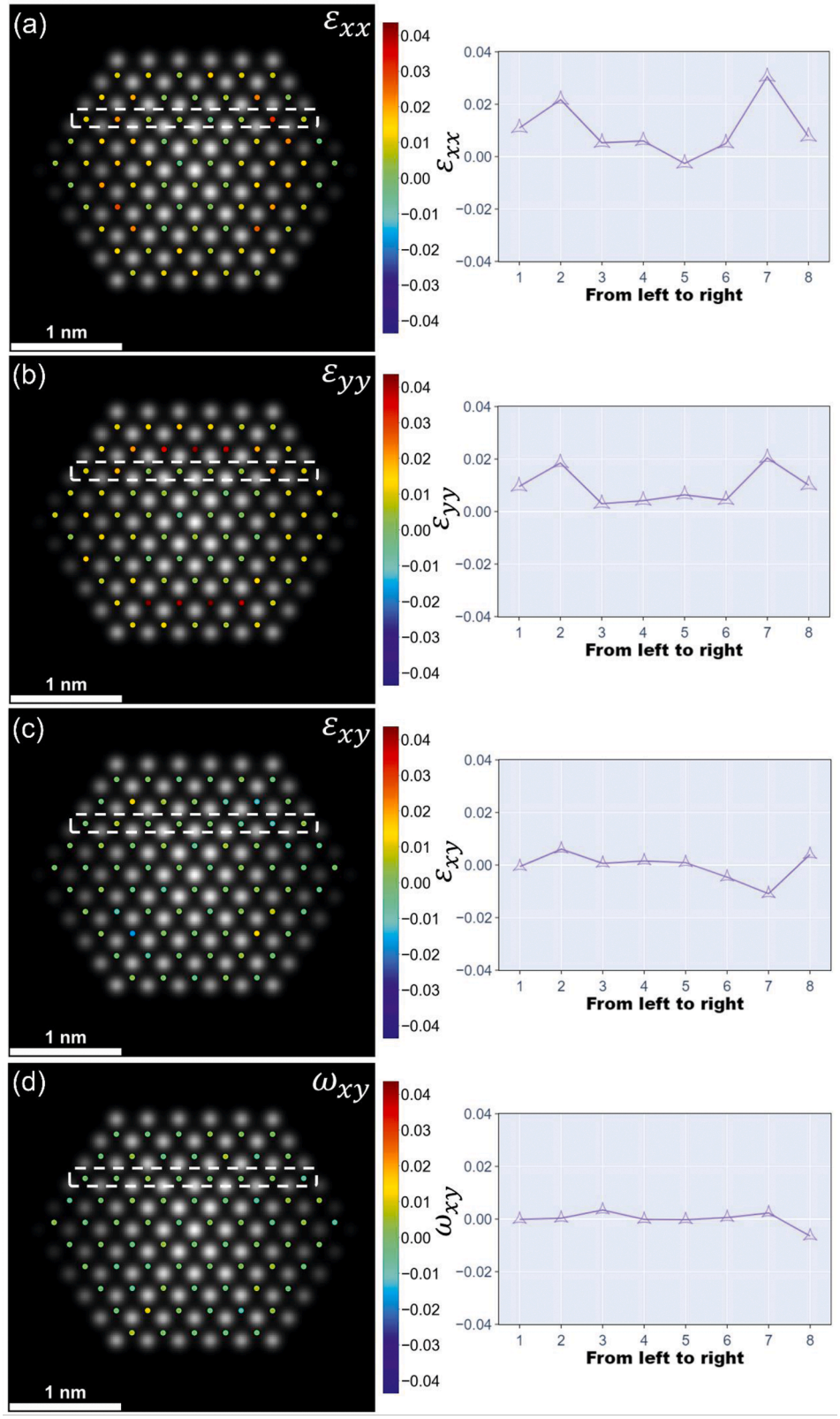

Fig. 5. The ε_{xx}, ε_{yy}, ε_{xy}, ω_{xy} maps and the corresponding line profiles of the strained Pt model.

$$\begin{aligned}\Delta \boldsymbol{u}_1 &= \boldsymbol{u}_1 - \boldsymbol{u}_0 \\ \Delta \boldsymbol{u}_2 &= \boldsymbol{u}_2 - \boldsymbol{u}_0\end{aligned} \tag{1}$$

Where $\boldsymbol{u}_0$, $\boldsymbol{u}_1$ and $\boldsymbol{u}_2$ are the displacement vectors of the atomic columns in each triangle and can be calculated using the position offsets between the observed and reference atomic columns. The differential displacement field is composed of vectors calculated between two nearest neighbour atomic columns along the two basis vectors. The two measured differential displacement vectors can be shown at the centre of each of the two basis vectors, respectively, as shown in Fig. 4c. Unlike

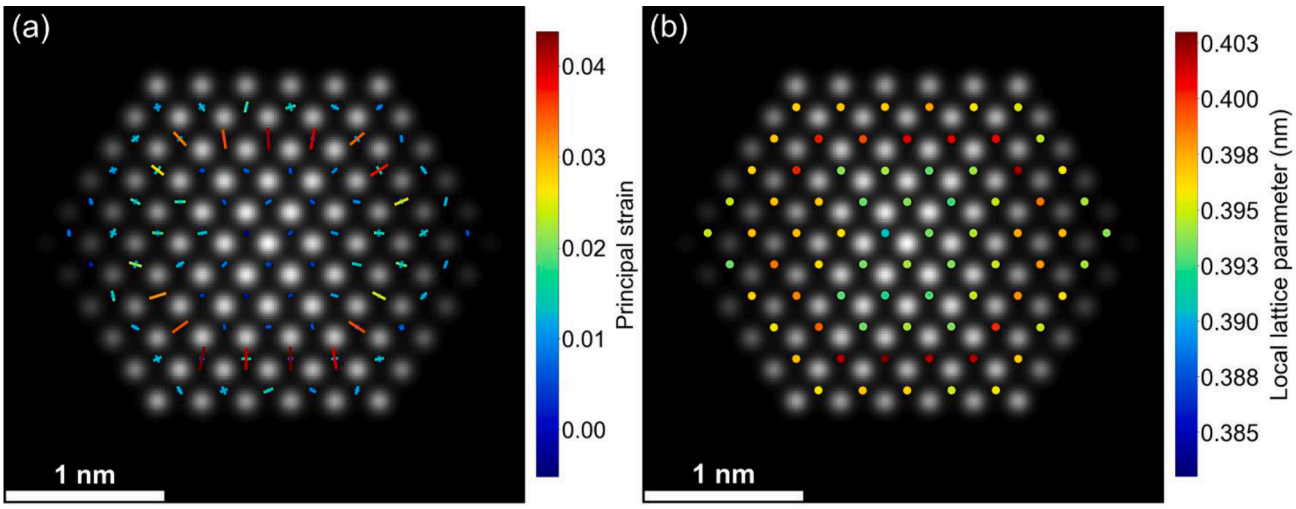

Fig. 6. The principle strain and local lattice parameter maps of the strained Pt model.

the displacement measurements where a zero-displacement region is required to fix the reference grid, the differential displacement measurements are robust to rigid-body shifts of the reference grid. Previous work has used the differential displacement maps to study atomic-scale deformation associated with dislocations [44,45]. If the measured differential displacement vectors ($\Delta\boldsymbol{u}_1$ and $\Delta\boldsymbol{u}_2$) are parallel to the basis vectors ($\boldsymbol{a}$ and $\boldsymbol{b}$), this indicates tensile strain. If the differential displacement vectors are antiparallel to the basis vectors, it indicates compressive strain. Shear strain exists when a differential displacement vector is perpendicular to its associated basis vector. Fig. 4d and e display the selected line profiles of the magnitude of the two differential displacement vectors. The selected atomic rows are along the directions of two basis vectors, respectively. Here, it can be seen that unlike the displacement distribution in Fig. 2a where the outermost layer has the largest displacement, the measured differential displacements peak between the second and third atomic layer. The main reason is that although the atoms in the surface atomic layer are displaced by 13 pm, the distance between the surface and second atomic layer only increases by 2.55 pm since the second atomic layer also moves outward the nanoparticle by 10.45 pm. However, in the centre row (Fig. 4f), the largest measured differential displacements are located between the third and fourth atomic layer. This is because the atomic column in the third atomic layer of the centre row only has 5 atoms, and four of them are the displaced atoms belonging to the two outer atomic shells due to the projection effect, as shown in Fig. 1e. As the result, this atomic column itself has a larger displacement compared to the other atomic column in the third atomic layer.

Based on the displacement field of the primitive triangle, we can have [28]:

$$\begin{aligned}\Delta u_{1x} &= a_x\varepsilon_{xx} + a_y e_{xy}\\ \Delta u_{1y} &= a_y\varepsilon_{yy} + a_x e_{yx}\\ \Delta u_{2x} &= b_x\varepsilon_{xx} + b_y e_{xy}\\ \Delta u_{2y} &= b_y\varepsilon_{yy} + b_x e_{yx}\end{aligned} \tag{2}$$

Where ε_{xx} and ε_{yy} are normal strains; a_x, a_y, b_x and b_y are the x and y components of the basis vectors **a** and **b** respectively. Shear strain (ε_{xy}) and lattice rotation (ω_{xy}) are defined as follows:

$$\begin{aligned}\varepsilon_{xy} &= \frac{1}{2}\left(e_{xy} + e_{yx}\right)\\ \omega_{xy} &= \frac{1}{2}\left(e_{xy} - e_{yx}\right)\end{aligned} \tag{3}$$

Because the differential displacement field in Eq. (2) can be written as a matrix multiplication, the expression can be inverted to give:

$$\begin{bmatrix}\varepsilon_{xx} & e_{xy}\\ e_{yx} & \varepsilon_{yy}\end{bmatrix} = \begin{bmatrix}\Delta u_{1x} & \Delta u_{2x}\\ \Delta u_{1y} & \Delta u_{2y}\end{bmatrix}\begin{bmatrix}a_x & b_x\\ a_y & b_y\end{bmatrix}^{-1} \tag{4}$$

Thus, the strain tensor for each primitive triangle is calculated using the differential displacement field and the reference basis vectors. Fig. 5 shows the measured strain maps alongside the selected line profiles of the strained Pt model. The first thing we can find is that the measured normal strains (ε_{xx} and ε_{yy}) peak between the second and third atomic layer. The reason has been explained in the differential displacement analysis. It indicates that unlike the displacement map in Fig. 2, both strain mapping and differential displacement mapping provide the local distortion information of the materials. The shear strain (ε_{xy}) and rotation (ω_{xx}) are smaller than the two normal strains, as might be expected from this simple dilation model. It can also be seen that the line profiles of the strain components are not perfectly symmetric. This is because unlike the radial displacements whose symmetric centre is the centre atom of the nanoparticle, use of the consistent basis vectors used for the strain calculation means that the two basis vectors do not represent symmetrically equivalent sides of the symmetrically related primitive triangles. Importantly, it can be seen that ε_{xx} mainly exists at the left and right sides of the strained nanoparticle, while ε_{yy} is mainly located at the top and bottom of the strained nanoparticle. This indicates that the two normal strain maps (ε_{xx} and ε_{yy}) can visualize the distortion behaviour of the materials along x and y directions but do not provide an overall measure of local deformation.

The principal strains ($\varepsilon_{\max}$ and $\varepsilon_{\min}$) are the maximum and minimum normal strains using a specific axis orientation where the shear strain is zero[46]. They can be calculated for each of the primitive triangles using the strain tensor components (ε_{xx}, ε_{yy} and ε_{xy}) using the following equations:

$$\varepsilon_{max} = \frac{1}{2}\left(\varepsilon_{xx} + \varepsilon_{yy}\right) + \sqrt{\left[\frac{1}{2}\left(\varepsilon_{xx} - \varepsilon_{yy}\right)\right]^2 + \varepsilon_{xy}^2} \tag{5}$$

$$\varepsilon_{min} = \frac{1}{2}\left(\varepsilon_{xx} + \varepsilon_{yy}\right) - \sqrt{\left[\frac{1}{2}\left(\varepsilon_{xx} - \varepsilon_{yy}\right)\right]^2 + \varepsilon_{xy}^2} \tag{6}$$

The orientation of the principal strain can be calculated by:

$$\tan 2\theta_p = \frac{2\varepsilon_{xy}}{\varepsilon_{xx} - \varepsilon_{yy}} \tag{7}$$

Where θ_p is the angle between the maximum principal strain and x axis. This equation gives two values of θ_p which are 90° apart, indicating that

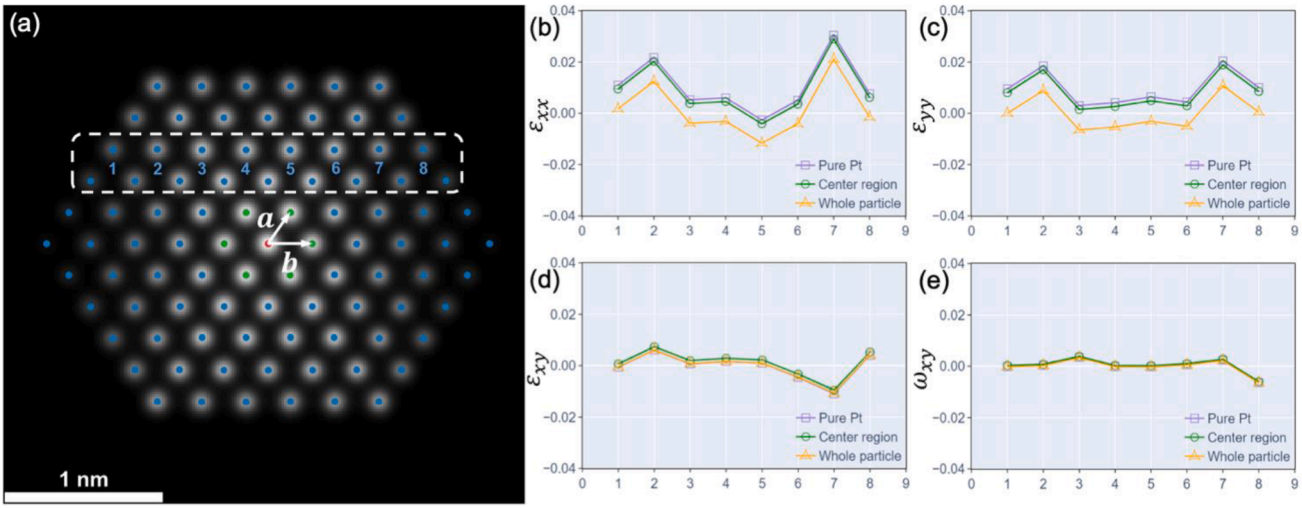

Fig. 7. (a) An initial triangle and a pair of basis vectors of the centre atom. Red: the centre atom; Green: the six neighbouring atoms; Blue: the observed atoms. (b-e) The line profiles of ε_{xx}, ε_{yy}, ε_{xy}, ω_{xy} in the selected region in (a) using the pure Pt crystal, centre region and whole particle to generate reference grids, respectively.

the two principal strain components are perpendicular to each other. Fig. 6a displays the principal strain map extracted from the normal and shear strain maps. The measured principal strains not only well-express the magnitude and orientation of the local strain configuration, but also are robust to both rigid-body shifts and rotations of the reference grid. In Fig. 6a, it demonstrates that the largest maximum principal strain is located between the second and third outer atomic layers, and is orientated outward the nanoparticle. The principle strain map carries the same information as that expressed by the conventional strain tensor components seen in Fig. 5, but provides a more intuitive view of the deformation in the nanoparticle. Note is that the measured principal strain between the first and second outer atomic layer is randomly orientated. This is because the measured ε_{xx} and ε_{yy} which are used for the orientation (θ_p) calculation in this region are small and close to each other, and therefore the orientation calculation is easily influenced by random displacements from the frozen phonon model used in the simulation.

In addition, the area change of each observed triangle with respect to the reference standard triangle can also be used to describe the distortion behaviour. The area of the reference triangle (S) can be computed by the following equation:

$$S = \frac{1}{2} \times a \times b \times \sin(\theta) \tag{8}$$

Where a and b are the length of two sides of the triangle, θ is the included angle. A differential can be applied to Eq. (8), to arrive at:

$$\frac{dS}{S} = \frac{da}{a} + \frac{db}{b} = \varepsilon_{xx} + \varepsilon_{yy} \tag{9}$$

It can be clearly seen that the fractional area expansion ($\frac{dS}{S}$) and $\varepsilon_{xx} + \varepsilon_{yy}$ are equivalent, which is a standard result in linear elasticity theory[46]. To first order, the area expansion does not depend on shear strain. Similarly, the average fractional local lattice parameter change ($\frac{dl}{l}$) can be defined as:

$$\frac{dl}{l} = \frac{1}{2}\left(\frac{da}{a} + \frac{db}{b}\right) \tag{10}$$

where l is the reference lattice parameter. Combining Eq. (9) and Eq. (10), this gives:

$$\frac{dl}{l} = \frac{1}{2}\left(\varepsilon_{xx} + \varepsilon_{yy}\right) \tag{11}$$

We now can write the local lattice parameter (l_{loc}) of each observed triangle as:

$$l_{loc} = l \times \left(\frac{1}{2}\left(\varepsilon_{xx} + \varepsilon_{yy}\right) + 1\right) \tag{12}$$

At this point, the distortion descriptors based on either the atomic column or the distortion triangle are successfully defined. The differential displacement components ($\Delta \boldsymbol{u}_1$ and $\Delta \boldsymbol{u}_2$) are the differential of the distortion along the two pre-defined basis vectors. The normal strains (ε_{xx} and ε_{yy}) can tell us about local compressive or tensile strain, along with the shear strain (ε_{xy}) and local lattice rotation (ω_{xy}), but are more intuitively expressed through the principal strains. The fractional area expansion, the sum of two normal strain components ($\varepsilon_{xx} + \varepsilon_{yy}$), the local lattice parameter (l_{loc}) and the average fractional local lattice parameter change ($\frac{dl}{l}$) tell us equivalent information for the distortion analysis on materials. It is important to note that the absolute values of the strain tensor components depend on the reference grid and its orientation. Rotation of the basis vectors can transform normal strains into shear strains and vice-versa. The principal strain is, however, independent of the rotation of the reference axes. It also describes the maximum normal strain that the local object can experience and its direction. The determination of the local lattice parameter does not rely on the reference grid, as shown in Fig. 6b. How the rotation, scaling and shearing of the reference grid influence the strain components will be explored next.

4. Choice of reference grid

In an experimental nanoparticle, the strain can be distributed throughout the particle due to its finite size and domain structure. It might not be possible to find a non-strained region in a small particle to generate the reference grid. In Section 3, it can be seen that the choice of the reference grid is crucial for the strain measurements. To investigate how the reference grid influences the strain analysis, three different reference grids were used for the strain mapping on the simulated image of the strained Pt model. The three different reference grids are the projected pure bulk Pt crystal lattice with a lattice constant of 0.39231 nm at 280 K [37], the grids refined from the whole particle and also the centre region of the particle. The centre region is defined as the centre atom and its six closest neighbouring atoms, as shown in Fig. 7a. The reason why pure bulk Pt crystal lattice is not always used as the reference grid is that a non-strained area in the experimental nanoparticle

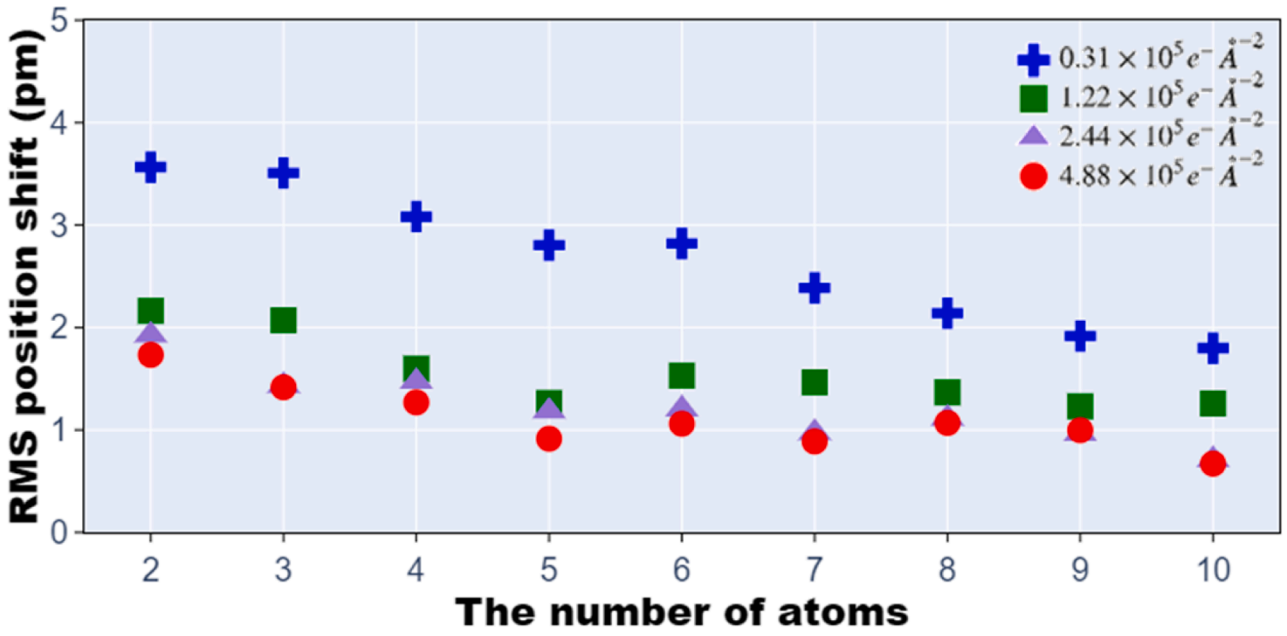

Fig. 8. The detected root mean square (RMS) position shift as a function of number of atoms in an atomic column in the simulated Poisson-distributed images of the perfect Pt model under the different electron doses.

might not be found to fix the pure bulk Pt crystal lattice due to its finite size. Rotation of pure Pt reference grid could affect displacement measurements. Thus, the other two grids derived from the nanoparticle were also considered for strain measurements.

Fig. 7b-e display the line profiles of each strain component from a same region of the nanoparticle. The line profile has eight primitive triangles (labelled from 1 to 8 in Fig. 7a), which are composed of the atoms in the outer four atomic layers. The distortion triangles 1 and 8 are from the first triangle layer, while the second triangle layer has the triangles 2 and 7. The rest of the triangles belong to the third triangle layer. The same variation can be observed in the strain maps using the three different reference grids, but the difference arising from using different reference grids for the strain measurements is a series of uniform offsets added to the measured strain components.

As mentioned before, the reference grid is created by periodically growing two reference basis vectors. Here, two different reference grids are described as $\boldsymbol{a}$ & $\boldsymbol{b}$ and $\boldsymbol{a}'$ & $\boldsymbol{b}'$ where the vectors denoted with primes are those that have some errors relative to correct unstrained basis vectors. The modified vectors can be defined by:

$$\begin{aligned} \boldsymbol{a}' &= \boldsymbol{T}\cdot\boldsymbol{a} \\ \boldsymbol{b}' &= \boldsymbol{T}\cdot\boldsymbol{b} \end{aligned} \tag{13}$$

Where $\boldsymbol{T}$ is a linear transformation matrix (scaling, shearing, rotation, etc.) to the reference grid. The differential displacement field in the $\boldsymbol{a}'$ & $\boldsymbol{b}'$ reference grid can be written as:

$$\begin{aligned} \Delta\boldsymbol{u}'_1 &= \Delta\boldsymbol{u}_1 + \boldsymbol{a} - \boldsymbol{a}' = \Delta\boldsymbol{u}_1 + (\boldsymbol{I} - \boldsymbol{T})\cdot\boldsymbol{a} \\ \Delta\boldsymbol{u}'_2 &= \Delta\boldsymbol{u}_2 + \boldsymbol{b} - \boldsymbol{b}' = \Delta\boldsymbol{u}_2 + (\boldsymbol{I} - \boldsymbol{T})\cdot\boldsymbol{b} \end{aligned} \tag{14}$$

Where $\boldsymbol{I}$ is the identity matrix. The strain component, ε_{xx} and ε_{yy} are found using Eq. (2). Because Eq. (14) shows that the effect of an error in the reference grid adds a constant to the differential displacement vector, it can be seen from Eq. (2) that it will also add a constant to each of the components of the strain tensor. Thus, we arrive at:

$$\begin{aligned} \varepsilon'_{xx} &= \varepsilon_{xx} + constant \\ \varepsilon'_{yy} &= \varepsilon_{yy} + constant \end{aligned} \tag{15}$$

This mathematic treatment can also be applied to the other strain components.

The scaling, shearing and rotation of the reference grid introduce additional erroneous apparent displacements that build up linearly with respect to the distance from the chosen origin of the reference lattice. However, the strain components are calculated by the derivative of the displacements (Eq. (2)). Thus, the change of the strain component equals the slope of the linear variation of the introduced extra displacement, which is a constant. To conclude, using different reference grids influences the absolute values of the measured strain components, but it only adds a series of uniform offsets to the results. The variation of the strain distribution is robust to the chosen of the reference grid.

5. Measurements reliability on noisy images

In previous sections, the strain measurements methodology has been introduced and its reliability on the simulated ADF image has been verified. The reliability of the strain measurements depends on the accuracy and precision of the atomic column position detection in the image. Thus, it is crucial to precisely determine atomic column positions, which is affected by the Poisson noise and scan instability. However, the multi-frame technique could be used to record multiple ADF frames with a shorted pixel dwell-time, to minimize the sample drift within each frame. By comparing the image frames, it is also possible to determine whether atom mobility introduced by the electron beam has influenced the precision of the atomic column position detection[47]. Those atomic columns where the atoms are moving would not be detected for the strain measurements. The obtained image stacks are aligned using the non-rigid registration technique to reduce the scan distortions and the resulting strain measurements have previously been compared and validated against the GPA approach[42,43,48].It has been reported that an uncertainty of 0.5 pm for the position detection on the averaged non-rigid registered ADF image can be achieved [40,49]. Here, we attempt to investigate the accuracy of our strain measurements on the simulated Poisson-distributed ADF images under different electron doses.

During a typical experimental data acquisition [42,50], around 16 ADF image frames with a total electron dose of ~4.88 × 10^5 e^- $Å^{-2}$ are obtained for the non-rigid alignment. In order to better understand the effect of the noise, Poisson noise under typically single-frame (0.31 × 10^5 e^- $Å^{-2}$), low (1.22 × 10^5 e^- $Å^{-2}$), medium (2.44 × 10^5 e^- $Å^{-2}$) and high

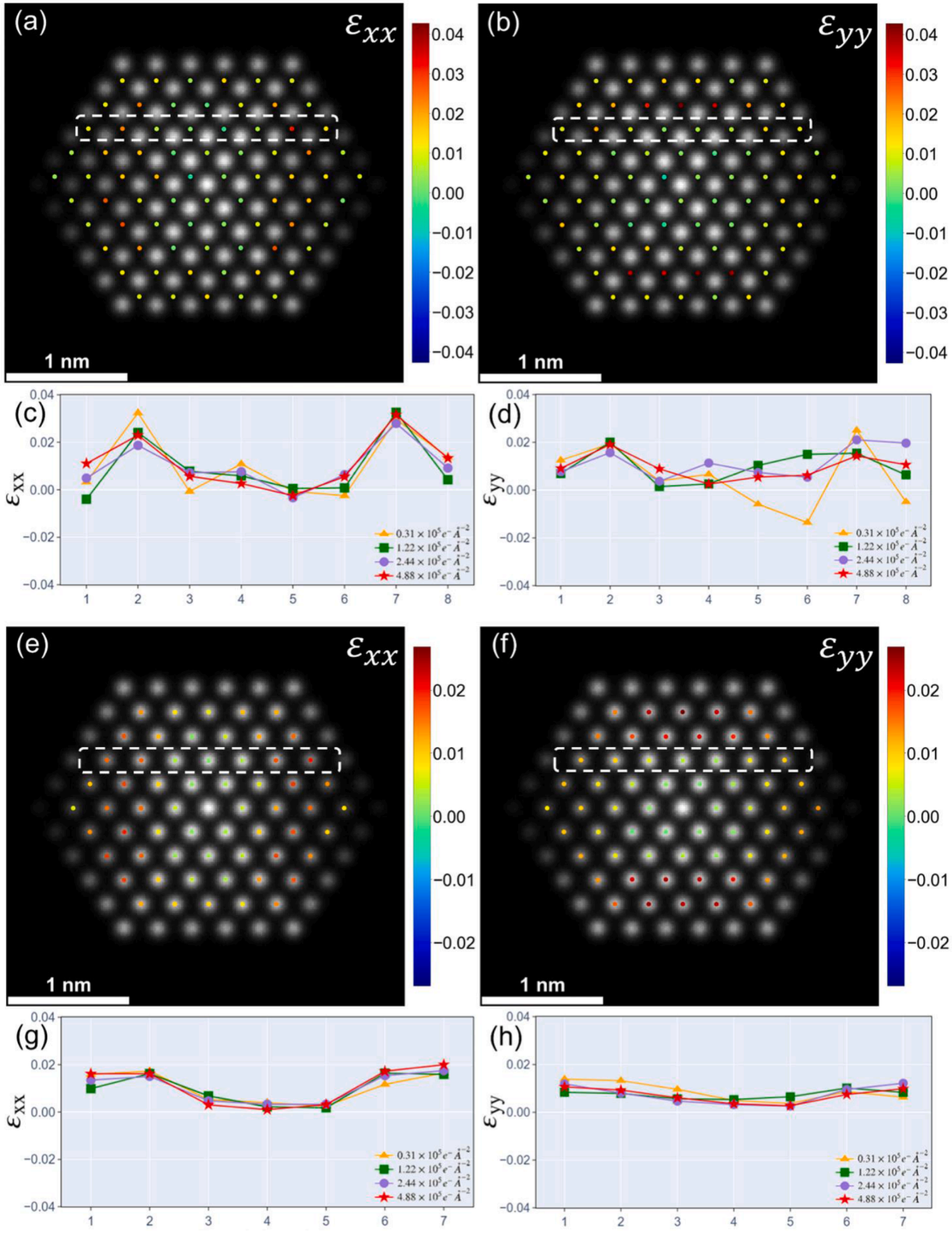

Fig. 9. The ε_{xx} and ε_{yy} maps from the simulated image of the strained Pt model with Poisson noise under the high electron dose, (a-b) measured using one neighbouring triangle, and (e-f) measured using six neighbouring triangles. The line profiles of ε_{xx} and ε_{yy} in the selected regions under different electron doses, (c-d) measured using one neighbouring triangle, and (g-h) measured using six neighbouring triangles.

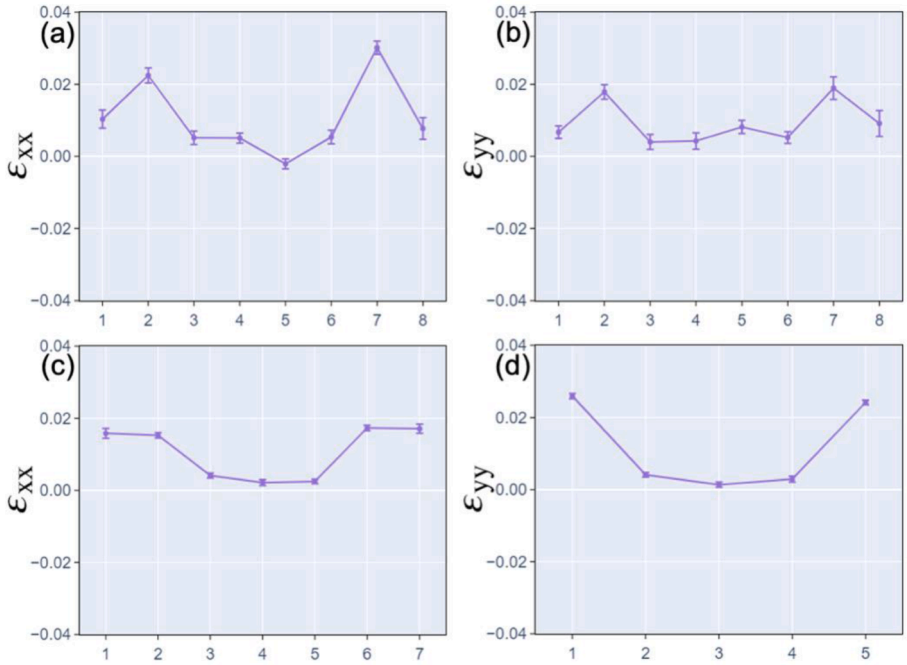

Fig. 10. Strain measurements on 10 simulated Poisson-distributed images under the high electron dose (4.88×10^5 e$^-$ Å^{-2}). The line profiles of averaged ε_{xx} and ε_{yy} in the selected regions in Fig. 9, (a-b) measured using one neighbouring triangle, (c-d) measured using six neighbouring triangles.

(4.88×10^5 e$^-$ Å^{-2}) electron doses, was added to the simulated ADF images of the perfect (zero-strain) and strained Pt models, respectively. The Poisson noise is added by replacing each pixel with a value selected randomly from a Poisson distribution with a mean given by the simulated number of electron counts. The determined atomic column positions in the simulated Poisson-distributed images of the perfect Pt model were compared with the real atom positions of the model averaged along a column, the distances between them are defined as the position shifts. Fig. 8 shows the measured RMS position shift as a function of number of atoms in an atomic column under the multiple noise realisations. For those atomic columns having more than 4 atoms, the accuracy of the atomic column position finding reaches 1 pm under the medium or high electron dose. The accuracy could be improved as the scattered intensity of the atomic column increases (higher electron dose or more atoms). The error of the length of the differential displacement vector can be calculated from the error of atomic column position detection using the error propagation theory[51], expressed as:

$$\Delta d = \sqrt{(\Delta d_1)^2 + (\Delta d_2)^2} = \sqrt{2}\ pm \tag{16}$$

Where Δd_1 and Δd_2 indicate the errors in the determination of the two atomic columns that constitute a differential displacement vector. Similarly, the error of strain calculation is mainly introduced by the error of the differential displacement measurement. Thus, the precision of strain measurements can be estimated by the equation:

$$\frac{\Delta \varepsilon}{\varepsilon} = \frac{\Delta d}{d} \tag{17}$$

Where d is the length of the differential displacement vector. For the differential displacement vectors chosen here, the precision of the strain measurements on STEM images is about 5×10^{-3}. It has been reported that the precision of strain mapping using the high-resolution transmission electron microscopy (HRTEM) images also could approach 10^{-3}. [20] However, compared to the TEM mode, STEM mode equipped with spectrometers allows for simultaneous local strain and composition analyses at atomic scale.

To investigate the electron dose influence on the strain analysis, the strain measurements were performed on the simulated images of the strained Pt model with different electron doses (and therefore, noise levels). The simulated images in Fig. 9a, b, e and f are under the high electron dose and purely used to illustrate the positions of the measured strains relative to the nanoparticle lattice. Fig. 9c and d shows how the measured normal strains can fluctuate from the actual ones under the different electron doses. For these plots, only one neighbouring triangle (as shown in Fig. 7) around each atomic column is used as the primitive unit for the measurements. The influence from the electron dose can be further reduced by sacrificing the spatial resolution of the strain analysis. All the neighbouring triangles of each atomic column (which are six triangles for the Pt model along the [110] projection) can be combined for the strain measurements [7]. The measured strain components from the six neighbouring triangles are then averaged and plotted at the atomic column, as shown in Fig. 9g and h. It can be clearly seen that the averaged normal strains using six primitive triangles are more robust to the electron dose.

To study the Poisson noise influence on the strain analysis under the high electron dose, the process of Poisson-distributed image simulation with the dose of 4.88×10^5 e$^-$ Å^{-2} was repeated 10 times. The strain measurements using one or six neighbouring triangles were then performed on these 10 simulated images, respectively. The line profiles of two averaged normal strain components with the standard deviations plotted as the error bars are compared in Fig. 10. Here, the standard deviation is calculated using the measured strain component of each atomic column from ten simulated Poisson-distributed images. A considerable reduction in the uncertainty is observed when averaging six neighbouring triangles for the strain measurements.

To conclude, an accuracy of 1 pm for the displacement measurements and a precision of 5×10^{-3} for the strain measurements can be achieved on the simulated Poisson-distributed images under the high electron dose used in this work. The electron dose and associated Poisson noise have a slight influence on the strain analysis. To improve the uncertainty of our measurements, an average over primitive cells can be taken, but the spatial resolution of the strain map will be reduced.

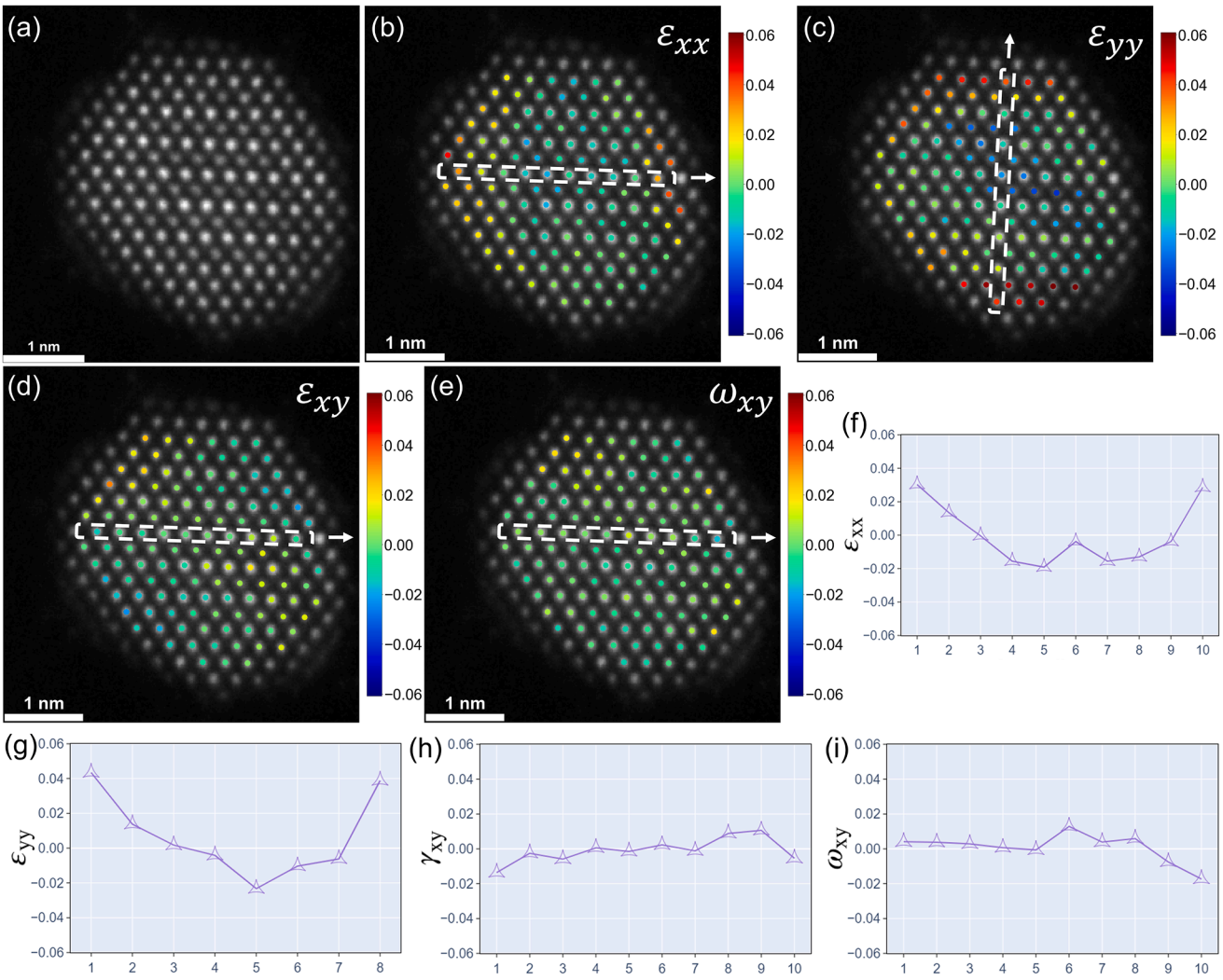

Fig. 11. (a) The atomic-resolution ADF STEM image of a $PtCo_3$ nanoparticle. The strain maps (b-e) of the particle and corresponding line profiles (f-i).

6. Application of the technique: de-alloyed $PtCo_3$ bimetallic nanoparticle

To demonstrate the potential of our proposed method, we applied the strain analysis method on a carbon supported de-alloyed $PtCo_3$ nanoparticle provided by Johnson Matthey plc. The $PtCo_3$ nanoparticles have been widely used as a catalyst for oxygen reduction reaction (ORR) in fuel cells due to the enhanced catalytic activity compared to the pure Pt. Precisely measuring the strain distribution at atomic scale within the $PtCo_3$ nanoparticles could help a better understanding of the intrinsic mechanism behind their catalytic enhancement. The TEM specimen was prepared by drop-casting the nanoparticles on a holey carbon grid and baked in vacuum for 8 h at 80 °C for hydrocarbon decontamination before imaging in the electron microscope. The vacuum pressure during the baking is about 1×10^{-7} mbar. The specimen was imaged using the STEM mode on a JEOL ARM 200F electron microscope fitted with a probe-forming aberration corrector. An operation voltage of 200 kV and a condenser lens aperture yielding a probe-convergence angle of 22.48 mrad were selected. The HAADF detector collection angles range from 72.8 to 271 mrad. The magnification of the microscope was calibrated using a UO_2 standard. To reduce scan distortion and minimise sample damage, 20 atomic-resolution ADF image frames with a short pixel dwell time of 4 μs and a pixel size of 0.0164 nm were recorded successively. Each image frame having 512 × 512 pixels was recorded under the beam current of 23.2 pA, yielding a total electron dose of about 4.3 $\times 10^5$ e^- $Å^{-2}$. The frames with good quality in the image stack were non-rigid aligned and averaged to improve SNR using the smart alignment software [43]. The strain analysis was performed on this nanoparticle using the reference grid refined from the whole particle using in-house developed code.

To extract local distortion information, the measured strain components were averaged using six neighbouring triangles around each atomic column and are shown in Fig. 11b-e. In the ε_{xx} map, the atoms on the left and right surfaces of the nanoparticle have the largest strain. In contrast, the largest ε_{yy} components mainly exist in top and bottom layers. It indicates that the atoms in outer atomic layers show larger interatomic distances than the average of the nanoparticle, but the appearance of large strain values is associated with the arbitrary choice of the x and y axes. The selected line profiles are plotted in Fig. 11f-i. Unlike the normal strains, the ε_{xy} and ω_{xy} components are quite small. The detected shear strain and lattice rotation on the surface layer may be introduced by the surface atom mobility.

Directly interpreting the distortion behaviour of the $PtCo_3$ nanoparticle from its displacement map in Fig. 12a is difficult because the displacement measurements are highly sensitive to the shift, rotation, shearing and scaling of the reference grid. Here, to improve the spatial resolution of the distortion analysis, only one triangle around each atomic column is used as a distortion unit. The results are therefore plotted at the centre of the triangles instead of the atomic columns. The differential displacement map in Fig. 12b shows that along the

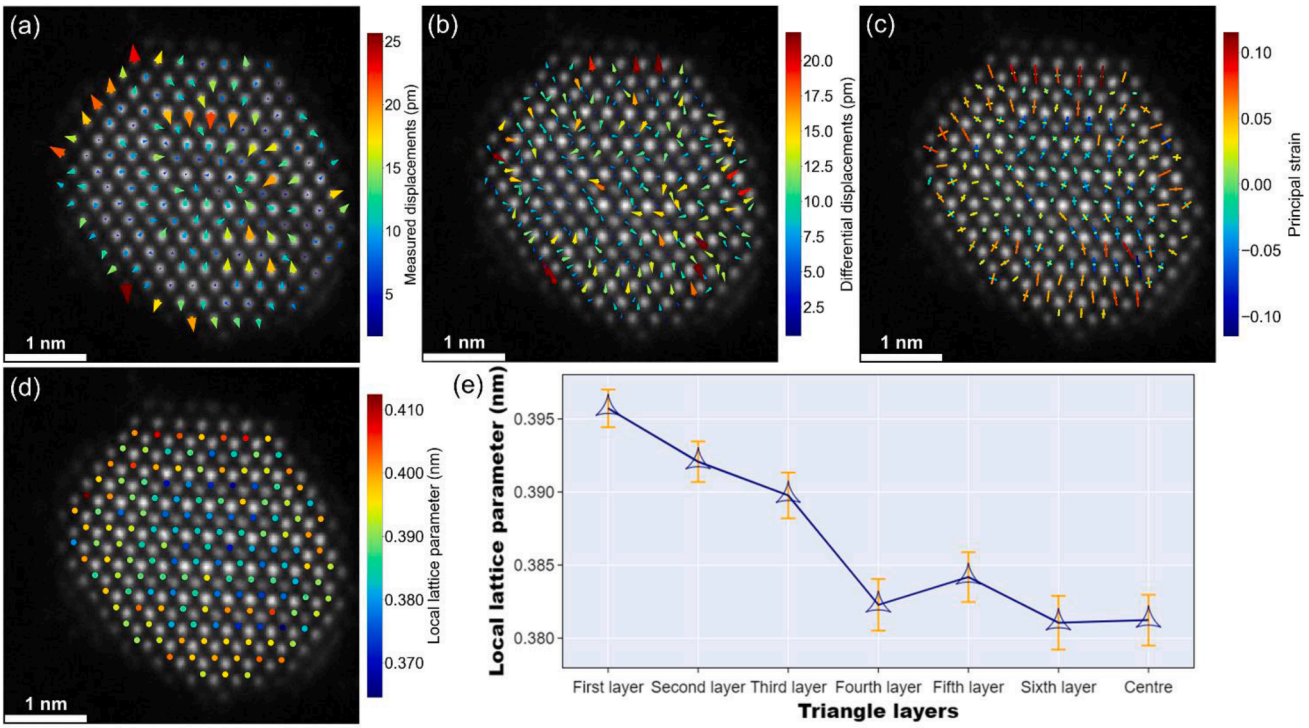

Fig. 12. (a) The measured displacement map, (b) the differential displacement map, (c) the principal strain map and (d) the local lattice parameter map of an experimental $PtCo_3$ nanoparticle. (e) The measured local lattice parameters vs triangle layers.

predefined basis vectors, tensile strain relative to the reference lattice is observed in the near-surface region while compressive strain dominates the centre region of the nanoparticle. The absolute values and directions of these differential displacements are independent of the rigid-body shift but affected by the rotation, shearing and scaling of the reference grid. The principal strain map of the nanoparticle (Fig. 12c) exhibits a similar distribution symmetry as that of the simulated strained Pt nanoparticle model in Fig. 6a. It indicates that atoms in the near-surface regions are dilated outwards relative to the reference lattice. Although the measured principal strain is robust to both the rigid-body shift and rotation, its absolute value still relies on the shearing and scaling of the reference grid. However, the measured local lattice parameters are absolute values that are independent of the reference grid, as long as the image magnification is accurate, as shown in Fig. 12d. Thus, the local lattice parameter can be directly compared between different Pt-Co species, and further used as a meaningful parameter to modelling for relating strain to catalytic activity.

To investigate the distortion variations from the surface to core of this nanoparticle, the measured local lattice parameter is plotted as a function of the triangle layer, as shown in Fig. 12e. Similar to the definition of the atomic layer, the triangle layers are defined as rings of primitive triangles moving from the surface to core of the nanoparticle, where the surface triangle layer is composed of those primitive triangles between the outermost and second atomic layers. Note is that the error bar of each triangle layer is demonstrated by the standard error. The first layer has more primitive triangles than the other layers, therefore it has the smallest standard error of the measured lattice parameter amongst the others. The local lattice parameter can be seen to increase approaching the particle surface. However, the local lattice parameters are uniformly distributed in the inner four triangle layers. One of the reasons might be that the finite size of the nanoparticle leads to surface lattice relaxations. In addition, the $PtCo_3$ nanoparticles have been reported to have a 'core-shell' effect on the composition distribution [16]. Thus, the composition variations across the nanoparticle are also considered as a contributor to its distortion behaviour. A detailed study correlating composition changes to strain is beyond the scope of this paper, but will be reported in a forthcoming paper.

7. Conclusions

In this work, first, it has been shown that the difference between the measured 2D displacements and the real projected 3D displacements of the strained layers for nanoparticles is sufficiently small to allow for the strain analysis from atomic-resolution ADF STEM images. A technique for the atomic site-specific deformation analysis on nanoparticles is then proposed. The variables defining the deformation of materials at atomic scale are presented and compared. The displacement vector on each atomic site is not effective for the local deformation analysis of nanoparticles because the measurements heavily rely on the shift, rotation, shearing and scaling of the reference grid. The differential displacement and strain tensor are robust to the rigid-body shift of the reference grid. Rotation of the reference grid can transform the normal strains to the shear strains (ε_{xy} and ω_{xy}), and vice-versa. Thus, measuring the strain tensor is not straightforwardly applied for the visualization of the local deformation behaviour of materials. The differential displacement ($\Delta \boldsymbol{u}_1$ and $\Delta \boldsymbol{u}_2$) can directly express the differential of the local distortion with both magnitude and direction. However, the principal strain ($\varepsilon_{\max}$ and $\varepsilon_{\min}$) is robust to both the rigid-body shift and rotation of the reference grid. It provides information about the maximum local normal strain and its direction. Unlike the other deformation parameters, the local lattice parameter that is independent of the reference grid, as long as the image magnification is accurate, is the absolute value of the local distortion, but it cannot give information about the distortion direction. Thus, measuring local lattice parameter together with either differential displacement or principal strain mapping enables us to comprehensively understand the distortion behaviour of nanoparticles.

Next, to understand how the rotation, shearing and scaling of the reference grid influence the strain tensor measurements, strain mapping on the simulated strained Pt nanoparticle using three different reference grids is compared. It has been found that although the absolute values of the strain components rely on the reference grid, the different reference grids only add a series of uniform offsets to the strain variations. Also,

the reliability of the proposed strain analysis approach on the simulated Poisson-distributed ADF images under the different electron doses is studied. The Poisson noise under the high electron dose has a negligible impact on atomic column position detection. A high accuracy of 1 pm for the displacement measurements and a precision of 5×10^{-3} for the strain measurements can be achieved under the commonly-used experimental conditions. This methodology is able to provide a robust strain analysis on the non-rigid aligned experimental ADF STEM images.

Finally, quantitative results of the strain analysis on an experimental $PtCo_3$ nanoparticle are reported. Compared with the centre of the nanoparticle, the presence of the expansion strain is mainly detected at the near-surface region. This deformation behaviour is likely introduced by the finite size and composition variations of the nanoparticle. The precise measurements of the local lattice parameter will significantly improve the comprehensive understandings in terms of the catalytic performance. In future works, the measured strain distribution will be related to local composition variations and catalytic activity of the Pt-Co nanoparticles.

Declaration of Competing Interest

The authors declare that they have no known competing financial interests or personal relationships that could have appeared to influence the work reported in this paper.

Acknowledgements

The authors thank Johnson Matthey for additional funding and provision of the Pt-Co samples. The authors also acknowledge the use of characterization facilities within the David Cockayne Centre for Electron Microscopy, Department of Materials, University of Oxford and in particular the EPSRC (EP/K040375/1 “South of England Analytical Electron Microscope”) and additional instrument provision from the Henry Royce Institute (Grant reference EP/R010145/1). Funding is also acknowledged from the EU H2020 Grant 823717 ESTEEM3).

References

[1] T. Toda, H. Igarashi, H. Uchida, M. Watanabe, Enhancement of the electroreduction of oxygen on Pt alloys with Fe, Ni, and Co, J. Electrochem. Soc. 146 (10) (1999) 3750.
[2] H.A. Gasteiger, N.M. Marković, Just a dream—Or future reality? Science 324 (5923) (2009) 48–49.
[3] R.M. Heck, R.J. Farrauto, S.T. Gulati, Catalytic Air Pollution control: Commercial Technology, John Wiley & Sons, 2016.
[4] J.X. Wang, H. Inada, L. Wu, Y. Zhu, Y. Choi, P. Liu, W.-.P. Zhou, R.R. Adzic, Oxygen reduction on well-defined core– shell nanocatalysts: particle size, facet, and Pt shell thickness effects, J. Am. Chem. Soc. 131 (47) (2009) 17298–17302.
[5] V. Stamenkovic, B.S. Mun, K.J. Mayrhofer, P.N. Ross, N.M. Markovic, J. Rossmeisl, J. Greeley, J.K. Nørskov, Changing the activity of electrocatalysts for oxygen reduction by tuning the surface electronic structure, Angew. Chem. 118 (18) (2006) 2963–2967.
[6] L. Gan, M. Heggen, R. O’Malley, B. Theobald, P. Strasser, Understanding and controlling nanoporosity formation for improving the stability of bimetallic fuel cell catalysts, Nano Lett. 13 (3) (2013) 1131–1138.
[7] T.N. Pingel, M. Jørgensen, A.B. Yankovich, H. Grönbeck, E. Olsson, Influence of atomic site-specific strain on catalytic activity of supported nanoparticles, Nat. Commun. 9 (1) (2018) 1–9.
[8] S.E. Temmel, E. Fabbri, D. Pergolesi, T. Lippert, T.J. Schmidt, Investigating the role of strain toward the oxygen reduction activity on model thin film Pt catalysts, ACS Catalysis 6 (11) (2016) 7566–7576.
[9] J. Wu, P. Li, Y.-T.F. Pan, S. Warren, X. Yin, H. Yang, Surface lattice-engineered bimetallic nanoparticles and their catalytic properties, Chem. Soc. Rev. 41 (24) (2012) 8066–8074.
[10] C. Solliard, M. Flueli, Surface stress and size effect on the lattice parameter in small particles of gold and platinum, Surf. Sci. 156 (1985) 487–494.
[11] P. Strasser, S. Koh, T. Anniyev, J. Greeley, K. More, C. Yu, Z. Liu, S. Kaya, D. Nordlund, H. Ogasawara, Lattice-strain control of the activity in dealloyed core–shell fuel cell catalysts, Nat. Chem. 2 (6) (2010) 454–460.
[12] L. Bu, N. Zhang, S. Guo, X. Zhang, J. Li, J. Yao, T. Wu, G. Lu, J.-.Y. Ma, D. Su, Biaxially strained PtPb/Pt core/shell nanoplate boosts oxygen reduction catalysis, Science 354 (6318) (2016) 1410–1414.
[13] S. Zhang, X. Zhang, G. Jiang, H. Zhu, S. Guo, D. Su, G. Lu, S. Sun, Tuning nanoparticle structure and surface strain for catalysis optimization, J. Am. Chem. Soc. 136 (21) (2014) 7734–7739.
[14] J. Aarons, L. Jones, A. Varambhia, K.E. MacArthur, D. Ozkaya, M. Sarwar, C.-.K. Skylaris, P.D. Nellist, Predicting the oxygen-binding properties of platinum nanoparticle ensembles by combining high-precision electron microscopy and density functional theory, Nano Lett. 17 (7) (2017) 4003–4012.
[15] J. Gavartin, M. Sarwar, D. Papageorgopoulos, D. Gunn, S. Garcia, A. Perlov, A. Krzystala, D.L. Ormsby, D. Thompsett, G. Goldbeck-Wood, Exploring Fuel Cell Cathode Materials: a High Throughput Calculation Approach, ECS Trans. 25 (1) (2009) 1335.
[16] T. Ellaby, A. Varambhia, X. Luo, L. Briquet, M. Sarwar, D. Ozkaya, D. Thompsett, P. D. Nellist, C.-.K. Skylaris, Strain effects in core–shell PtCo nanoparticles: a comparison of experimental observations and computational modelling, Phys. Chem. Chem. Phys. 22 (42) (2020) 24784–24795.
[17] D. Cooper, T. Denneulin, N. Bernier, A. Béché, J.-.L. Rouvière, Strain mapping of semiconductor specimens with nm-scale resolution in a transmission electron microscope, Micron 80 (2016) 145–165.
[18] P. Jones, G. Rackham, J.W. Steeds, Higher order Laue zone effects in electron diffraction and their use in lattice parameter determination, Proc. R. Soc. Lond. A. Math. Phys. Sci. 354 (1677) (1977) 197–222.
[19] D. Diercks, G. Lian, J. Chung, M. Kaufman, Comparison of convergent beam electron diffraction and geometric phase analysis for strain measurement in a strained silicon device, J. Microsc. 241 (2) (2011) 195–199.
[20] M.J. Hÿtch, A.M. Minor, Observing and measuring strain in nanostructures and devices with transmission electron microscopy, MRS Bull. 39 (2) (2014) 138.
[21] A. Toda, H. Nakamura, T. Fukai, N. Ikarashi, Channel strain in advanced complementary metal–oxide–semiconductor field effect transistors measured using nano-beam electron diffraction, Japan. J. Appl. Phys. 47 (4S) (2008) 2496.
[22] M. Naito, M. Ishimaru, Y. Hirotsu, M. Takashima, Local structure analysis of Ge-Sb-Te phase change materials using high-resolution electron microscopy and nanobeam diffraction, J. Appl. Phys. 95 (12) (2004) 8130–8135.
[23] A. Lubk, E. Javon, N. Cherkashin, S. Reboh, C. Gatel, M. Hÿtch, Dynamic scattering theory for dark-field electron holography of 3D strain fields, Ultramicroscopy 136 (2014) 42–49.
[24] M. Hÿtch, F. Houdellier, F. Hüe, E. Snoeck, Nanoscale holographic interferometry for strain measurements in electronic devices, Nature 453 (7198) (2008) 1086–1089.
[25] D. Cooper, J.-.L. Rouviere, A. Béché, S. Kadkhodazadeh, E.S. Semenova, K. Yvind, R. Dunin-Borkowski, Quantitative strain mapping of InAs/InP quantum dots with 1 nm spatial resolution using dark field electron holography, Appl. Phys. Lett. 99 (26) (2011), 261911.
[26] M. Hÿtch, E. Snoeck, R. Kilaas, Quantitative measurement of displacement and strain fields from HREM micrographs, Ultramicroscopy 74 (3) (1998) 131–146.
[27] M. Hÿtch, T. Plamann, Imaging conditions for reliable measurement of displacement and strain in high-resolution electron microscopy, Ultramicroscopy 87 (4) (2001) 199–212.
[28] P.L. Galindo, S. Kret, A.M. Sanchez, J.-.Y. Laval, A. Yanez, J. Pizarro, E. Guerrero, T. Ben, S.I. Molina, The Peak Pairs algorithm for strain mapping from HRTEM images, Ultramicroscopy 107 (12) (2007) 1186–1193.
[29] R. Bierwolf, M. Hohenstein, F. Phillipp, O. Brandt, G. Crook, K. Ploog, Direct measurement of local lattice distortions in strained layer structures by HREM, Ultramicroscopy 49 (1–4) (1993) 273–285.
[30] P. Bayle, T. Deutsch, B. Gilles, F. Lançon, A. Marty, J. Thibault, Quantitative analysis of the deformation and chemical profiles of strained multilayers, Ultramicroscopy 56 (1–3) (1994) 94–107.
[31] P. Galindo, J. Pizarro, S. Molina, K. Ishizuka, High resolution peak measurement and strain mapping using peak pairs analysis, Microsc. Anal.-UK (130) (2009) 23.
[32] J.-.M. Zuo, A.B. Shah, H. Kim, Y. Meng, W. Gao, J.-.L. Rouviére, Lattice and strain analysis of atomic resolution Z-contrast images based on template matching, Ultramicroscopy 136 (2014) 50–60.
[33] K.-.J. Hanszen, Method of off-axis electron holography and investigations of the phase structure in crystals, J. Phys. D Appl. Phys. 19 (3) (1986) 373.
[34] M.J. Hÿtch, J.-.L. Putaux, J.-.M. Pénisson, Measurement of the displacement field of dislocations to 0.03 Å by electron microscopy, Nature 423 (6937) (2003) 270–273.
[35] K. Usuda, T. Numata, T. Irisawa, N. Hirashita, S. Takagi, Strain characterization in SOI and strained-Si on SGOI MOSFET channel using nano-beam electron diffraction (NBD), Mater. Sci. Eng.: B 124 (2005) 143–147.
[36] B. Goris, J. De Beenhouwer, A. De Backer, D. Zanaga, K.J. Batenburg, A. Sánchez-Iglesias, L.M. Liz-Marzán, S. Van Aert, S. Bals, J. Sijbers, G. Van Tendeloo, Measuring lattice strain in three dimensions through electron microscopy, Nano Lett. 15 (10) (2015) 6996–7001.
[37] J. Arblaster, Crystallographic properties of platinum, Platinum Met. Rev. 41 (1) (1997) 12–21.
[38] I. Lobato, D. Van Dyck, MULTEM: a new multislice program to perform accurate and fast electron diffraction and imaging simulations using Graphics Processing Units with CUDA, Ultramicroscopy 156 (2015) 9–17.
[39] H. Gao, L.-.M. Peng, Parameterization of the temperature dependence of the Debye–Waller factors, Acta Crystallogr. Sect. A Found. Crystallogr. 55 (5) (1999) 926–932.
[40] M. Nord, P.E. Vullum, I. MacLaren, T. Tybell, R. Holmestad, Atomap: a new software tool for the automated analysis of atomic resolution images using two-dimensional Gaussian fitting, Adv. Struct. Chem. Imag. 3 (1) (2017) 1–12.
[41] D. Van Dyck, M.O. De Beeck, A simple intuitive theory for electron diffraction, Ultramicroscopy 64 (1–4) (1996) 99–107.

[42] L. Jones, S. Wenner, M. Nord, P.H. Ninive, O.M. Løvvik, R. Holmestad, P.D. Nellist, Optimising multi-frame ADF-STEM for high-precision atomic-resolution strain mapping, Ultramicroscopy 179 (2017) 57–62.
[43] L. Jones, H. Yang, T.J. Pennycook, M.S. Marshall, S. Van Aert, N.D. Browning, M. R. Castell, P.D. Nellist, Smart Align—A new tool for robust non-rigid registration of scanning microscope data, Adv. Struct. Chem. Imag. 1 (1) (2015) 1–16.
[44] E. Clouet, Ab initio models of dislocations, Handb. Mater. Model.: Methods: Theory Model. (2020) 1503–1524.
[45] V. Vitek, R. Perrin, D. Bowen, The core structure of ½ (111) screw dislocations in bcc crystals, Philos. Mag. 21 (173) (1970) 1049–1073.
[46] B.J. Goodno, J.M. Gere, Mechanics of Materials, Cengage learning, 2020.
[47] A. De Backer, L. Jones, A. Varambhia, P.D. Nellist, S. Van Aert, Measuring dynamic structural changes of nanoparticles at the atomic scale using scanning transmission electron microscopy, Phys. Rev. Lett. 124 (10) (2020), 106105.
[48] L. Jones, P.D. Nellist, Identifying and correcting scan noise and drift in the scanning transmission electron microscope, Microsc. Microanal. 19 (4) (2013) 1050.
[49] A.B. Yankovich, B. Berkels, W. Dahmen, P. Binev, S.I. Sanchez, S.A. Bradley, A. Li, I. Szlufarska, P.M. Voyles, Picometre-precision analysis of scanning transmission electron microscopy images of platinum nanocatalysts, Nat. Commun. 5 (1) (2014) 1–7.
[50] A. De Backer, G. Martinez, K. MacArthur, L. Jones, A. Béché, P. Nellist, S. Van Aert, Dose limited reliability of quantitative annular dark field scanning transmission electron microscopy for nano-particle atom-counting, Ultramicroscopy 151 (2015) 56–61.
[51] L. Lyons, L. Louis, A Practical Guide to Data Analysis For Physical Science Students, Cambridge University Press, 1991.